

*Chapter 3*

# DIGITAL HOLOGRAPHY FOR THREE-DIMENSIONAL METROLOGY: PRINCIPLES, METHODS AND APPLICATIONS

*Chao Zuo<sup>1,\*</sup>, Qian Chen<sup>1</sup>, Weijuan Qu<sup>3</sup> and Anand Asundi<sup>2</sup>*

<sup>1</sup>Jiangsu Key Laboratory of Spectral Imaging and  
Intelligence Sense, Nanjing University of Science and Technology,  
Nanjing, Jiangsu Province, China

<sup>2</sup>Centre for Optical and Laser Engineering,  
School of Mechanical and Aerospace Engineering,  
Nanyang Technological University, Singapore

<sup>3</sup>Centre for Applied Photonics and Laser Technology,  
Ngee Ann Polytechnic, Singapore

## Abstract

In this chapter, we present the basic principle and recent developments of digital holography for applications in Micro-Electro-Mechanical System (MEMS) structure and device inspection, micro-optics characterization, and quantitative phase contrast bio-imaging. Different types of recording geometries and reconstruction algorithms of digital holography are reviewed. We also present several experimental results that demonstrate the capabilities of digital holography for various applications in science and engineering. For material science, micro- and nanotechnologies,

---

\*E-mail address: [surpasszuo@163.com](mailto:surpasszuo@163.com)

MEMS and microsystem, digital holography is performing almost ideally in many conditions: it can provide precise, absolute, and calibrated data, rendering possible the quantitative comparison with a certain gauge and standard; it can be designed compact enough which allow measurements being made on-line during the fabrication stage; it can be rapidly adapted to changing requirements because of its flexibility provided by digital processing. For micro-optics testing, digital holography offers the great advantage in measuring small lens structures with a very compact and simple geometry. Several biological applications, such as morphology and functional studies are presented, proving that digital holographic microscopy can bring quantitative phase information with fast imaging capabilities, non-scanning and non-invasive features.

## 1. Introduction

Holography, invented in 1947 by the Hungarian physicist Dennis Gabor (1), is a two-step imaging technique comprises the successful combination of interferences and diffraction. As illustrated in Fig. 1, the interferences encode the amplitude and the phase information of the object wave simultaneously and the diffraction acts as a decoder which reconstructs a wave which seems to be formed from the previously illuminated object. As the etymology of the word “holography” suggests, a hologram contains all the necessary information of the object, holography has been widely applied in optical metrology since not only the intensity but also the optical phase and therefore the depth and contours of the object can be recovered. However, the cumbersome procedures and stringent requirements on equipment in traditional holography such as the use of photographic plates for recording, wet chemical treatment, and physical illuminating, significantly restricted its practical applications.

Work presented by Konrod et al. (2) in 1972 was the first attempt to replace the silver photo plate with a matrix of holographic discrete values and then reconstruction to be performed by numerical calculation. At the time, it took 6 hours of calculation to reconstruct a field of pixels, using the Minsk-22 computer. The discrete values were obtained from a plate hologram by 64 bit digitization with a scanner. From that time period on, microtechnological processes have enabled detector matrices with sufficiently miniaturized pixels to be obtained in order to respond to the Shannon criteria concerning the discretisation of the spatial distribution of light (3). On the other hand, the computerized processing of images became accessible thanks, in the most part, to the notable

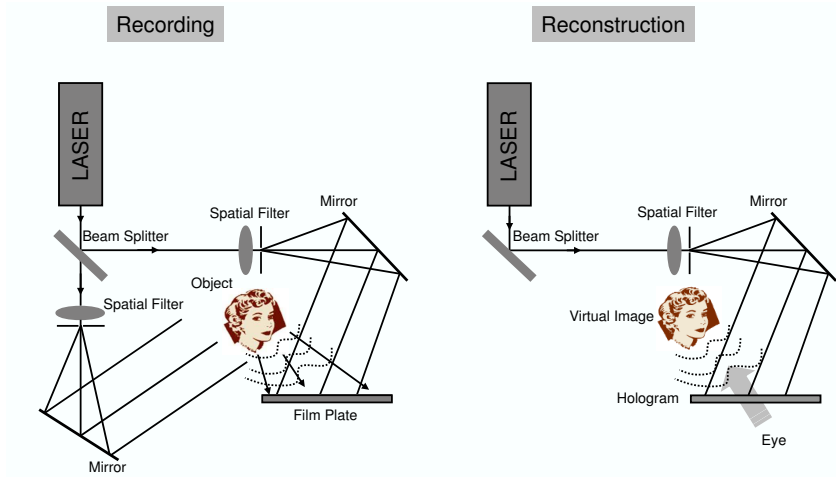


Figure 1. Recording and reconstruction in conventional holography.

improvement in the performance of microprocessors, particularly in their processing power as well as in their virtual memory space.

The idea of “digital holography” that to replace the analogue recording and decoding of the object with a digital recording/decoding process simulating a diffraction from the recorded image now has become a reality. In comparison with traditional holography, the main advantages of digital holography is that the hologram can be directly recorded by a digital imaging device, making chemical processing unnecessary. Besides, the intensity as well as phase information of a holographically stored wavefront can be retrieved directly and quantitatively through the numerical reconstruction process realized by a computer. The capability of whole field information storage in a hologram and the use of computer technology for fast data processing offer more flexibilities in experimental configuration and significantly increase the speed of the experimental process, opening up a lot of possibilities to develop digital holography as a novel metrological tool. Over the past two decades, the use of digital holography for three-dimensional (3D) surface measurement and quantitative phase imaging has become one of the most active research areas in optical metrology. There has been an enormous progress in digital holography systems development and methodologies and moreover, this technique has found various applications in diverse fields of science and engineering: characterization of MEMS compo-

nents (4, 5, 6), vibration analysis (7, 8, 9, 10), displacement and deformation measurement (11, 12), material analysis (13), surface profilometry (14, 15, 16), image encryption and information security (17, 18), measurement of micro-optics (19, 20), lensless imaging (21, 22), quantitative phase contrast imaging (23, 24), 3D object recognition (25, 26), extending depth-of-field (27, 28), particle imaging and velocimetry for flow field (29, 30, 31, 32), 3D microscopy (33, 34), aberration compensation (35, 36, 37, 38), tomographic 3D imaging (39, 40), 3D display (41, 42, 43), just to cite a few.

In this article, we conduct a brief review of digital holography including its basic principles, key methodologies, and typical applications. In Section 2, the two steps in digital holography - digital recording and numerical reconstruction are thoroughly discussed respectively in Sections 2.1 and 2.2. The different optical configurations for digital holographic recording are introduced in Section 2.1.1. In the digital recording process, hologram is recorded onto a CCD or other digital recording devices. The limited resolution of commercially available CCD sensors pose some restrictions on the recording geometry, which are investigated in Section 2.1.2. As is presented in Section 2.2.1, in the numerical reconstruction stage, suppressing the zero-order and the twin image is the first step to ensure reliable phase retrieval of the object wave. Then the object wavefield is numerically propagated from the hologram plane to the image plane based on diffraction theory of wave propagation, which is reviewed in Section 2.2.2. After numerical reconstruction, the complex object wavefield in digital form can be obtained. Direct manipulations of the deduced amplitude and phase for the numerical correction of aberrations are introduced in Section 2.2.3. In Section 3, we focus on three typical applications of digital holography in MEMS and microsystem metrology (Section 3.1), characterization of micro-optics (Section 3.2), and quantitative phase contrast bio-imaging (Section 3.3), respectively. Finally, summary and perspectives are given in Section 4.

## 2. Principle

“Digital” holography differs from “analogue” holography in terms of the recording materials which are used and in the image reconstruction process for the studied object. So generally, the digital holography technique can be divided into two parts: digital recording and numerical reconstruction, as shown in Fig. 2. In the digital recording process, a “digital hologram” of the object is recorded using different optical configurations onto a CCD or other digital recording de-

VICES. While during the numerical reconstruction process, the phase and amplitude information of the object are carried out by the digital simulation of wave diffraction in the “digital hologram”.

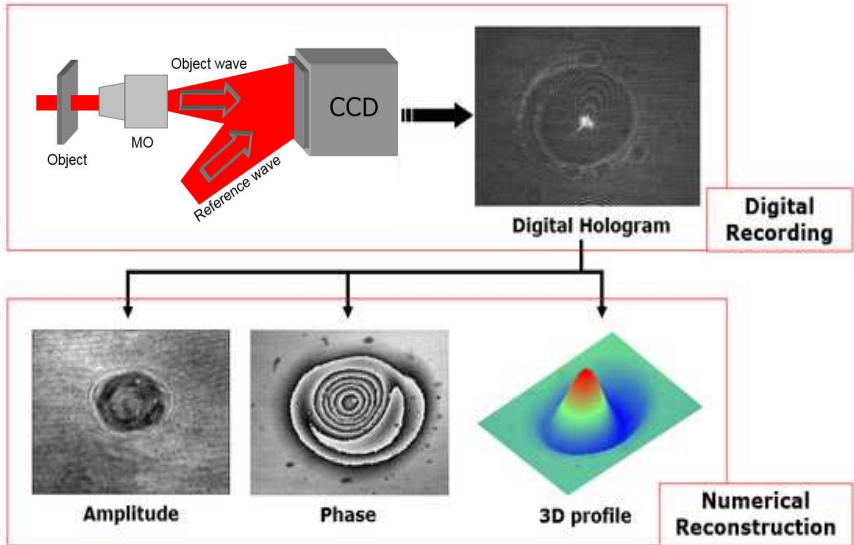


Figure 2. Digital recording and numerical reconstruction in digital holography.

## 2.1. Digital Recording

### 2.1.1. Recording Geometry

There are different setups for recording holograms. In general, they can be classified into a variety of types from different standpoints. Since the digital hologram can be interpreted as an interferogram of the object beam and the reference beam, considering whether there exist a tilt angle between the two beams, we can classify the recording setups into two main generic types: in-line holography and off-axis holography. In-line holography can be further divided into two modes. The first mode is so-called Gabor holography wherein only one illumination beam is used. Part of the beam scattered by the object serves as object beam and the other part of light unaffected by the object serves as reference beam. In the other mode, one beam is split into reference beam and object beam which illuminates the object. At the recording device, these two

beams interfere with each other with no tilt angle between the two beams. In off-axis holography, one beam is split into reference beam and object beam by a beam splitter or a fiber coupler and finally recombined at the recording device with a tilt angle. The drawback of in-line holography is that both the undiffracted reference beam and object beam are in the same direction. Thus, the in-focus image is always overlapped by the out-of-focus image (so-called twin images). Therefore, the phase shifting technique is needed to determine the phase and separate the twin images. The off-axis arrangement can overcome this drawback in nature. We will discuss this point detailedly in Section 2.2.1.

Holography can also be classified into reflection mode and transmission mode according to the different ways that light interacts with the object. If the optical information recorded by the hologram is reflected by the object, the system is characterized as reflection holography. If the optical information recorded by the hologram is transmitted through the object, the system is characterized as transmission holography. Holography can be also divided into lensless holography and holography with lens. If no lens is used in the system or lenses are used but not to manipulate the object wave after it interacts with object, the system is a lensless holography system. If lens or microscope objective is used to generate object image and to improve the lateral resolution, the system can be called digital holography microscope. Based on the distance between the object and hologram or between the focused object image and hologram when imaging lens is used, holography can be divided into image-plane holography, Fresnel holography and Fraunhofer holography. If the distance between the in-focus object and the hologram is zero, it is called image-plane holography system. If the distance is in the Fresnel diffraction region, it is called Fresnel holography system. If the distance is very large, extending to the Fraunhofer diffraction region, such system is called Fraunhofer holography system.

### 2.1.2. Digital Sampling of the Hologram

The main advantage of digital photosensitive material is that the image is acquired quickly without having the chemical development stage, which represents a considerable time gain. Another advantage is that these plates are reusable once the data is stored. Whatever digital recording device is used, the hologram  $I_H(x, y)$  will be converted into a discrete two-dimensional array  $I'_H(x', y')$  which consist of  $N \times M$  pixels at a pitch of  $\Delta x \times \Delta y$  ( $x' = 0, 1, \dots, N - 1$  and  $y' = 0, 1, \dots, M - 1$ ). The fill-factors of the pixels in x and y

directions are  $\alpha, \beta \in [0, 1]$ . Figure 3 depicts the pixel matrix, and the digitally sampled holograms can be written as

$$I'_H(x', y') = \left[ I_H(x, y) \otimes \text{rect} \left( \frac{x}{\alpha \Delta x}, \frac{y}{\beta \Delta y} \right) \right] \times \text{rect} \left( \frac{x}{N \Delta x}, \frac{y}{M \Delta y} \right) \text{comb} \left( \frac{x}{\Delta x}, \frac{y}{\Delta y} \right). \quad (1)$$

Here  $\text{rect}(x/\alpha \Delta x, y/\beta \Delta y)$  represents a single two-dimensional pixel of the CCD. The  $\otimes$  represent the two-dimensional convolution which describe the integration effect of one-single detector. The  $\text{rect}(x/N \Delta x, y/M \Delta y)$  stands for the finite size of the whole sensor chip. The periodic appearance of pixels is expressed by the convolution with the comb-function  $\text{comb}(x/\Delta x, y/\Delta y)$ .

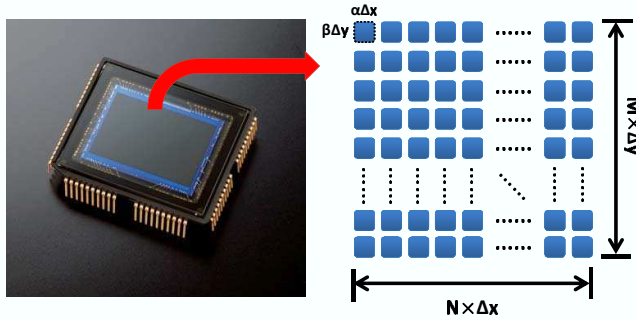


Figure 3. Schematics to show the sampling effect of the CCD pixels.

We should notice that, the spatial discretization of the recorded pattern and the dimensions of the pixel elements impose certain conditions on the recording of a hologram. As shown in Fig. 4, considering a simple case when the interference fringes generated by two monochromatic plane waves, at an angle of  $\theta$  apart, have an inter-fringe distance of  $\Delta p$ :

$$\Delta p = \frac{\lambda}{2 \sin(\theta/2)}. \quad (2)$$

The Shannon theorem indicates that for the correct acquisition of a given periodic signal, the sample frequency must be at least twice as high as the signal frequency. Otherwise, there would be a loss of information due to the pixel aliasing. In another words, the angle should must be not too large in order that

the inter-fringe distance corresponds to at least 2 pixels in digitally acquiring hologram

$$\theta_{\max} \leq 2\sin^{-1} \left( \frac{\lambda}{4 \max \{ \Delta x, \Delta y \}} \right). \quad (3)$$

For a wavelength of 633nm and a pitch between the pixels of  $4.65\mu m$ , the maximum angle, corresponding to the limits of the Shannon criteria, is about  $3.9^\circ$ . The small angular deviation which is thus permitted between the two beams requires the use of a relatively precise adjustment device. Remember the reality has turned out to be more complicated since the object wave is actually a diffracted wave rather than a plane wave so the maximum inter-fringe distance is object-dependent.

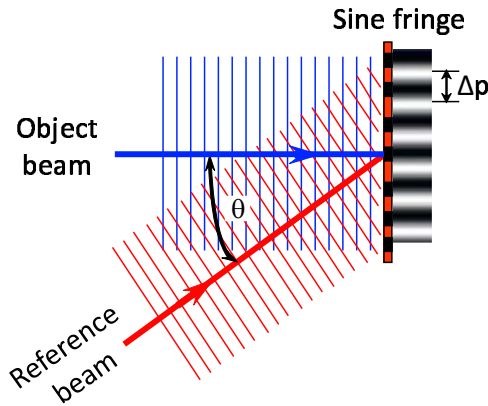


Figure 4. The local density of the fringe is proportionate to the relative angle between the object beam and the reference beam.

## 2.2. Numerical Reconstruction

The intensity distribution of the recorded hologram can be written as:

$$I_H(x, y) = |O|^2 + |R|^2 + RO^* + R^*O, \quad (4)$$

where  $R(x, y)$  and  $O(x, y)$  are the reference and object waves respectively,  $*$  denotes the complex conjugate. In this format, it is easy to explain the three components of a hologram. The 0-order, or dc-term  $|O|^2 + |R|^2$  is the sum

of the squares of the modules of the two waves. The -1-order  $RO^*$  is also called the real image; it is directly proportional to the conjugate complex of the object wave. This image is pseudoscopic, taking into account its inverted contours (phase conjugation/retroreflection). The +1-order  $R^*O$  is also called the virtual image, which is the most adapted to observation given that it is directly proportional to the original complex field. The real image  $RO^*$  and the virtual image  $R^*O$ , which combined are called the twin images. Only one of the twin-images is required to reconstruct a hologram and retrieve the object wave.

**2.2.1. Suppress the Zero-order and the Twin Image**

In off-axis digital holography removing the zero-order and twin-image is generally trivial, this is because the three terms are separated in the spatial frequency domain and one or the other can be removed through a band-pass filter (44). If we assume a reference wave with an relative angular shift  $\theta$ , which has the form  $R(x, y) = |R| \exp(-ik \sin \theta x)$ , then the intensity distribution of the hologram becomes

$$I_H(x, y) = |O|^2 + |R|^2 + |R| O \exp(-ik \sin \theta x) + |R| O^* \exp(ik \sin \theta x). \quad (5)$$

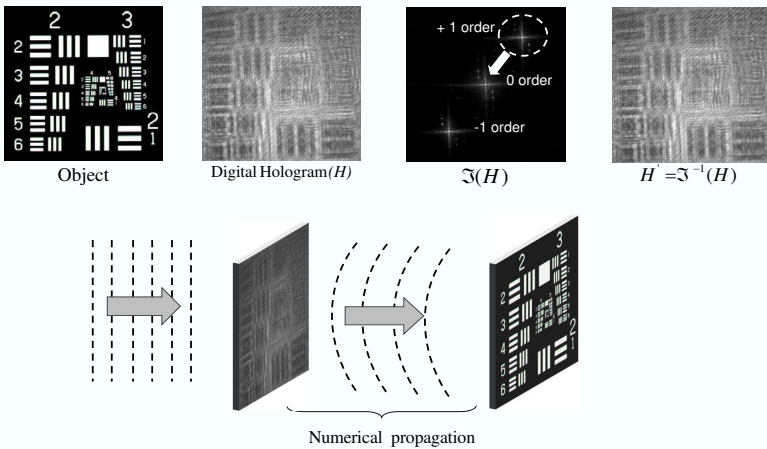


Figure 5. Numerical reconstruction process for an off-axis hologram.

If we now consider the Fourier transform of the hologram intensity, the influence of the two phase factors  $\exp(\pm ik \sin \theta x)$  can be interpreted as a transla-

tion of the spatial frequencies associated with the real and the virtual images: the spatial frequencies of the zero order of are located in the center of the Fourier plane, while the spatial frequencies of the interference terms vary at different carrier frequencies, which are located symmetrically with respect to the center of the Fourier plane:  $-k \sin \theta / 2\pi$  for the virtual image and  $k \sin \theta / 2\pi$  for the real image. This suggests that the different terms of the reconstructed wave front can be spatially filtered. This whole process is displayed in Fig. 5, where the new filtered hologram  $I_f(x, y)$  is defined by

$$I_f(x, y) = |R| O \exp(-ik \sin \theta x) = \mathcal{F}^{-1} \{ \mathcal{F} \{ I_f(x, y) \} \times H(u, v) \} \quad (6)$$

The Fourier transform and its inverse are denoted by  $\mathcal{F}$  and  $\mathcal{F}^{-1}$ , which is usually implemented by the fast Fourier transform (FFT).  $(\xi, \eta)$  is the vector in frequency space corresponding to  $(x, y)$ . The function  $H$  is the transfer function of the spatial filter, which should eliminate all spatial frequencies except those of the virtual interference term wanted. To avoid suppression of the high-frequency components of the virtual terms, the support of  $H$  should be chosen as large as possible. Smoothed transfer function profiles such as Gaussian, Hamming, or Hanning windows can be used to avoid the Gibbs effect in the reconstructed images, which may arise if parts of the spectrum of the real or of the virtual image are truncated.

In in-line digital holography configuration, however, the situation is more complex since the three orders are superimposed and the virtual image is thus mixed with the real image and the direct transmission of the reference beam. They are also held within the same area in the spatial frequency domain, so simple spatial filtering will not remove either one. Twin-image removal and suppression is a complicated and well-researched area, and there is no individually accepted method for removing the twin-image for in-line digital holography. The most well adopted method is phase-shifting which requires the recording of multiple independent holograms with different phase shift in the reference beam (45). These can be achieved by using a piezoelectric transducer (PZT) actuated mirror or a phase spatial light modulator (SLM) controlled by a computer. Assuming that the intensity reference wavefront is a constant, the interference intensity with phase-shift  $\delta_n$  can be represented by

$$I_n(x, y) = |O|^2 + |R|^2 + 2 \operatorname{Re} [OR \cdot \exp(i\delta_n)] \quad (7)$$

Here  $\operatorname{Re}[*]$  stands for getting the real part of the complex number. In conventional N-step phase shifting algorithms,  $\delta_n = 2\pi n/N$ , where  $n$  is the number

of the phase shift  $n = 1, 2, 3, \dots, N$ . By considering the above simultaneous formulas, the phase can be solved as (46)

$$\Delta\phi(x, y) = \tan^{-1} \frac{\sum_{n=1}^N I_n(x, y) \sin(2\pi n/N)}{\sum_{n=1}^N I_n(x, y) \cos(2\pi n/N)}, \quad (8)$$

Where  $\Delta\phi$  is the phase difference between the object beam and the reference beam. To solve the  $\Delta\phi$  uniquely, at least 3 phase shift steps are required. For example, in the most commonly used four-step phase-shifting procedure, the reference phase is shifted by a step of  $\pi/2$  four times, the phase difference

$$\Delta\phi(x, y) = \tan^{-1} \left( \frac{I_4(x, y) - I_2(x, y)}{I_1(x, y) - I_3(x, y)} \right). \quad (9)$$

Then the twin images has been well separated, and the complex amplitude of the virtual image can be solved by

$$R^*O = \frac{1}{4} \{I_4(x, y) - I_2(x, y) + j [I_1(x, y) - I_3(x, y)]\}. \quad (10)$$

In real applications, the phase shift number  $N$  should be chosen properly, by considering the accuracy and noise level of the measurement. Generally, the larger  $N$  is, a more accurate phase can be retrieved. After tens of years development, the phase shifting algorithms have already formed a complete theoretical system. For conventional  $N$ -step phase shifting algorithms, their behaviors, like sensitivities to random noise, phase shift errors, intensity nonlinearity error, etc. have been studied exhaustively (47, 48, 49). In some specific applications, the phase shifting algorithm can even be customized to minimize the given error sources (48, 49).

### 2.2.2. Numerical Propagation the Wavefront

Once we obtain the +1-order  $R^*O$ , a numerical representation of the original reference wave can be multiplied to the processed hologram to obtain the complex object wavefront  $O$  at the hologram plane (for the case when the reference wavefront is a collimated wave with constant intensity, this step can be simply omitted due to the form of  $R^*$  is only a constant). However, the real amplitude and phase of the object, is located at the object plane  $-d$  away from the hologram plane. Therefore, a numerical propagation based on diffraction theory

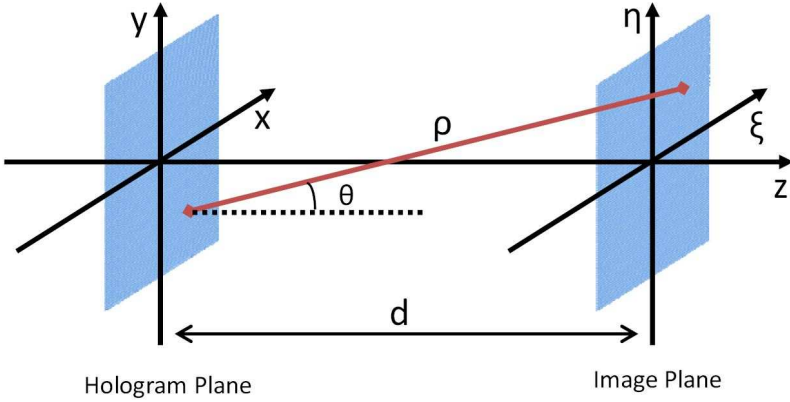


Figure 6. The coordinate system to describe the wave propagation.

should be performed to play the wave back to its original position in order to get the intensity and the phase of the object wavefield precisely.

With the coordinate system of Fig. 6, the diffraction of a light wave at the hologram plane is described by the Huygens-Fresnel principle or Fresnel-Kirchhoff formula as (50)

$$\Gamma(\xi, \eta) = \frac{1}{j\lambda} \int_{-\infty}^{+\infty} \int_{-\infty}^{+\infty} O(x, y) \frac{\exp(jk\rho)}{\rho} \cos \theta dx dy, \quad (11)$$

with

$$\rho = \sqrt{(x - \xi)^2 + (y - \eta)^2 + d^2}, \quad (12)$$

where  $\Gamma(\xi, \eta)$  is the object wavefront at image plane propagated from the hologram plane and  $\rho$  is the distance between a point in the hologram plane and a point in the reconstructed image plane, as shown in Fig. 6. The angle  $\theta$  is also shown in Fig. 6. From geometry  $\cos \theta = d/\rho$  and substituting into Eq. (11),  $\Gamma(\xi, \eta)$  can be written as

$$\Gamma(\xi, \eta) = \frac{d}{j\lambda} \int_{-\infty}^{+\infty} \int_{-\infty}^{+\infty} O(x, y) \frac{\exp(jk\rho)}{\rho^2} \cos \theta dx dy. \quad (13)$$

Equation (13) is the basis for numerical hologram reconstruction. As the reconstructed wavefield  $\Gamma(\xi, \eta)$  is a complex function, both the intensity as well as the phase of the object can be determined quantitatively. Though the direct

calculation the integration of Eq. (13) is quite time-consuming and memory-demanding, it can be efficiently implemented based on FFT under Fresnel approximation, or considering Eq. (13) as a convolution, or recasting Eq. (13) from the angular spectrum point-of-view. The Fresnel approximation is based on the binomial expansion of Eq. (13) with the assumption that the  $x$  and  $y$  values as well as  $\xi$  and  $\eta$  values are small compared to  $d$ , which reduces Eq. (13) to the form

$$\Gamma(\xi, \eta) = \frac{\exp(jk\rho)}{j\lambda d} \int_{-\infty}^{+\infty} \int_{-\infty}^{+\infty} O(x, y) \exp \left\{ \frac{j\pi}{\lambda d} [(x - \xi)^2 + (y - \eta)^2] \right\} dx dy. \quad (14)$$

If we expand the exponential term and pull the irrelevant variables out of the integral, Eq. (14) can be represent as

$$\begin{aligned} \Gamma(\xi, \eta) &= \frac{\exp(jk\rho)}{j\lambda d} \exp \left[ \frac{j\pi}{\lambda d} (\xi^2 + \eta^2) \right] \\ &\int_{-\infty}^{+\infty} \int_{-\infty}^{+\infty} O(x, y) \exp \left[ \frac{j\pi}{\lambda d} (x^2 + y^2) \right] \exp \left[ -\frac{j2\pi}{\lambda d} (x\xi + y\eta) \right] dx dy. \end{aligned} \quad (15)$$

The Eq. (15) is referred as the Fourier representation of the Fresnel diffraction since it can be evaluated as an Fourier transform if we assume  $u = \xi/\lambda d$ , and  $v = \eta/\lambda d$ . Alternatively, Eq. (13) can also be written as a convolution if the  $\cos \theta = d/\rho \approx 1$

$$\Gamma(\xi, \eta) = \int_{-\infty}^{+\infty} \int_{-\infty}^{+\infty} O(x, y) g(\xi - x, \eta - y) dx dy = O(x, y) * g(x, y), \quad (16)$$

where the impulse response  $g(x, y)$  is given by

$$g(x, y) = \frac{1}{j\lambda} \frac{\exp \left( jk \sqrt{x^2 + y^2 + d^2} \right)}{\sqrt{x^2 + y^2 + d^2}}. \quad (17)$$

The convolution of Eq. (16) can be calculated by using FFT according to the convolution theorem,

$$\Gamma(\xi, \eta) = \mathcal{F}^{-1} \{ \mathcal{F} \{ O(x, y) \} \mathcal{F} \{ g(x, y) \} \}. \quad (18)$$

The Fourier transform of the impulse response function  $G(u, v)$  is called transfer function. From the angular spectrum view point, the transfer function  $G$

should have the following form

$$G(u, v) = \mathcal{F} \{g(x, y)\} = \exp \left[ ikd \sqrt{1 - (\lambda u)^2 - (\lambda v)^2} \right], u^2 + v^2 < \lambda^{-1} \quad (19)$$

Thus we have

$$\Gamma(\xi, \eta) = \mathcal{F}^{-1} \{ \mathcal{F} \{O(x, y)\} G(u, v) \}. \quad (20)$$

This saves one Fourier transform compared with Eq. (18). It should be noted that under Fresnel approximation, the transfer function  $G$  becomes

$$G_F(u, v) = \mathcal{F} \{g(x, y)\} = \exp(jkd) \exp[-j\pi\lambda d(u^2 + v^2)] \quad (21)$$

Put Eq. (21) into Eq. (18), and represent it as a convolution, we have

$$\begin{aligned} \Gamma(\xi, \eta) &= O(x, y) * g_F(x, y) \\ &= \frac{\exp(jk\rho)}{j\lambda d} \int_{-\infty}^{+\infty} \int_{-\infty}^{+\infty} O(x, y) \exp \left\{ \frac{j\pi}{\lambda d} [(x - \xi)^2 + (y - \eta)^2] \right\} dx dy. \end{aligned} \quad (22)$$

in which

$$g_F(x, y) = \frac{\exp(jkd)}{j\lambda d} \exp \left[ \frac{j\pi}{\lambda d} (x^2 + y^2) \right]. \quad (23)$$

The numerical implementation of Eqs. (15), (18), and (20) are referred as Fresnel transform method, convolution method, and angular spectrum method, respectively. These three methods are most widely used method in digital holography reconstruction. Actually, there are even two more methods since the transfer function in angular spectrum method can be replaced by its Fresnel approximation [Eq. (21)] and the impulse response in convolution approach can also be approximated by its Fresnel counterpart Eq. (23).

Assuming a  $N \times M$  hologram with the sampling intervals  $\Delta x$  and  $\Delta y$ , the reconstructed object field at a distance  $d$  should also be the matrix of  $N \times M$  which describes the complex amplitude distribution of the real image and with sampling intervals  $\Delta \xi$  and  $\Delta \eta$ . All the five different numerical implementations of the diffraction integral are summarized in Table 1. Among these method, the angular-spectrum method is most widespread used in digital holography, because it offers several advantages, including maintaining the pixel size, rigorously satisfying the scalar wave equation, and no minimum distance requirement for the reconstruction plane.

**Table 1. Numerical implementations of the diffraction integral for digital holographic reconstruction.**

Method	Category	Algorithm	Impulse Response/ Transfer function	Sampling interval	FFT times
Fresnel transform	Direct integration	$\Gamma = z \mathcal{F}\{O\}$	$z(m, n) = \exp\left[j\frac{\pi}{\lambda d}\left(m^2 \Delta x^2 + n^2 \Delta y^2\right)\right]$ $c(k, l) = \exp\left[j\frac{\pi}{\lambda d}\left(k^2 \Delta x^2 + l^2 \Delta y^2\right)\right]$	$\Delta z = \frac{\lambda d}{N \Delta x}$ $\Delta \eta = \frac{\lambda d}{M \Delta y}$	1
Convolution	Convolution based on impulse response	$\Gamma = \mathcal{F}^{-1}\{\mathcal{F}\{O\} \mathcal{F}\{g\}\}$	$g(k, l) = \frac{1}{j\lambda} \frac{\exp\left\{jk\sqrt{(k\Delta x)^2 + (l\Delta y)^2 + d^2}\right\}}{\sqrt{(k\Delta x)^2 + (l\Delta y)^2 + d^2}}$	$\Delta z = \Delta x$ $\Delta \eta = \Delta y$	3
Fresnel approximation based convolution	Convolution based on impulse response	$\Gamma = \mathcal{F}^{-1}\{\mathcal{F}\{O\} \mathcal{F}\{g_f\}\}$	$g_f(k, l) = \frac{\exp(jkd)}{j\lambda d} \exp\left\{j\frac{\pi}{\lambda d}\left[(k\Delta x)^2 + (l\Delta y)^2\right]\right\}$	$\Delta z = \Delta x$ $\Delta \eta = \Delta y$	3
Angular frequency	Convolution based on transfer function	$\Gamma = \mathcal{F}^{-1}\{\mathcal{F}\{O\} G\}$	$G(m, n) = \exp\left[ikd \sqrt{1 - \left(\lambda \frac{m}{N \Delta x}\right)^2 - \left(\lambda \frac{n}{M \Delta y}\right)^2}\right]$	$\Delta z = \Delta x$ $\Delta \eta = \Delta y$	2
Fresnel approximation based angular frequency	Convolution based on transfer function	$\Gamma = \mathcal{F}^{-1}\{\mathcal{F}\{O\} G_f\}$	$G_f(m, n) = \exp(jkd) \exp\left[-j\pi \lambda d \left(\frac{m^2}{N^2 \Delta x^2} + \frac{n^2}{M^2 \Delta y^2}\right)\right]$	$\Delta z = \Delta x$ $\Delta \eta = \Delta y$	2

### 2.2.3. Aberration Compensation

Assuming an ideal case that the reference and object wave without the presence of specimen are assumed to be plane waves, and the specimen modulates the intensity and introduces a phase delay  $\phi(x, y)$  resulting from a height difference of the specimen in reflection configuration or from a refractive index or/and thickness difference in transmission configuration, the virtual image term extracted can be represented by

$$RO^* = |R| |O| \exp(i\phi). \quad (24)$$

Therefore, both the intensity and the phase of the object can be reconstructed accurately if the wavefield is numerical propagated back to the original location of the object plane. Now let us consider a more general case that the reference and object wave without the presence of specimen are not perfectly plane waves, but with additional phase aberration  $W_R$  and  $W_{O'}$ , respectively.

$$R = |R| \exp(iW_R), \quad (25)$$

and

$$O' = |O'| \exp(iW_{O'}). \quad (26)$$

the object wave diffracted by the specimen can be represented as

$$O = |O| \exp(i\phi) \cdot \exp(iW_{O'}). \quad (27)$$

Then the virtual image terms extracted becomes

$$RO^* = |R| |O| \exp(i\phi) Q(x, y), \quad (28)$$

where  $Q(x, y)$  is the phase aberration term that needs to be compensated, which is determined by the phase difference between the reference wave and undiffracted object wave

$$Q(x, y) = \exp[i(W_{O'} - W_R)]. \quad (29)$$

The most common aberration in digital holographic microscopy is the off-axis tilt and the defocus associated with the use of a microscope objective. As we have discussed in Section 2.2.1, the off-axis tilt introduces a linear phase factor in the virtual image terms, which only translates the spatial frequencies associated with the real and the virtual images from the center of the Fourier plane to higher frequencies domain. The main propose of introducing a microscope objective in the object arm is to increases the transverse resolution of the digital holography system, produce a magnified image of the object at the hologram plane. However, the objective induces quadratic wavefront distortion, which influences only the phase but not the amplitude image. Considering these two types of aberration, the phase aberration term can be general which can be generally represented by

$$Q(x, y) = \exp[i(k_x x + k_y y)] \exp[i(l_x x^2 + l_y y^2)], \quad (30)$$

where the factors  $k_x, k_y$  denote the linear phase difference between  $O$  and  $R$  due to the off-axis geometry. The parameters  $l_x, l_y$  in Eq. (30) describe the relative divergence between the object and reference beam due to the mismatch in spherical phase curvature. A lot of work has been done in recent years to compensate the phase aberration in digital holographic microscopy in order to accurately recover the phase information induced by the object only. They can be categorized into two groups: physical (23, 37, 51) and numerical (35, 52, 36, 53, 54, 38, 14). The basic idea behind physical methods is to introducing the same curvature in the reference beam to nullify the effect of aberration in the objective. It can be achieved by using a same objective lens in the reference arm, located at the same distance as in the object beam (23), or introducing an adjustable lens to manually flatten the wavefront by changing its position in the reference arm (37). If the quadratic aberration is completely eliminated and there is no test object, the spectra of the virtual image should be a shifted delta function with sharp

point distribution (52, 37). Therefore, one can simply monitor the shape of the spectrum to judge whether the spherical phase curvature is totally compensated during the setup alignment process.

It should be noted that only the defocus aberration can be physically compensated and the tilt aberration can only be corrected numerically (unless one really wants to change the recording setup from off-axis type to in-line type). Fortunately, in the absence of defocus aberration, tilt correction can be realized by a simple spectrum centering procedure – locate the amplitude maximum corresponding to the central frequency of the virtual image spectrum and then shift it to the center of the spectrum image (see Fig. 5). This procedure has been shown quite effective in most cases and can be easily incorporated into the spatial filtering and the numerical reconstruction steps without the need of additional Fourier transform (52, 37). However, it is noteworthy that this method has three main drawbacks: first, the precision of this method is limited to only one-pixel, second, this method is based on the assumption that the zero frequency is the dominant frequency component of the object, which may be not true if the object is complex or demonstrates significant periodicity. Finally, if the phase curvature is not completely eliminated, the spectrum will no longer demonstrate a punctual central frequency which makes the spectrum centering difficult.

The major drawback of the physical methods is they require a precise alignment or adjustment of the optical elements involved and a perfect wavefront curvature matching between the object and reference arms is difficult to realize in practice. Alternatively, the phase aberration can be removed during post-processing of the digital hologram by numerical methods. In general, the task of phase aberration compensation is to find a phase term which can be directly multiplied to the hologram or subtracted from the final reconstructed phase map to counteract the effect of the aberration term  $Q(x, y)$ , therefore, the numerical compensation method can be further classified into hologram plane methods and image plane methods. The compensation term, which is also called phase mask or compensation phase factor, can be obtained by manual adjustment (14, 55), exploiting some pre-knowledge about the setup (35, 14, 55), using an additional reference hologram without the specimen (36, 35), low-pass filtering the hologram spectrum (36), applying 1-D curve fitting (52), 2D standard spherical surface fitting (54), Zernike polynomials fitting (53), etc.

Compared with the image plane approaches, compensation in the hologram plane avoids the need of adapting the phase mask when the reconstruction distance is changed (36, 37). Furthermore, phase aberrations at the hologram plane

will partially convert into intensity distortion during wave propagation. Compensation in hologram plane can avoid such kind of image distortion. However, extracting the phase mask or compensation phase factor at the hologram plane involve 2D phase unwrapping which is found difficult since the object field is out-of-focus. Besides, the additional reconstruction, unwrapping, as well as the 2D fitting resides on the large computational requirements which make them costly from a processing and computational point-of-view, precluding real-time monitoring. Recently, a simple and effective numerical phase aberration compensation method based on principal component analysis (38) is proposed to overcome these difficulties. A close inspection of Eq. (30) reveals that the ideal model for  $Q(x, y)$  is in fact a rank one matrix. This allows the definition of two vectors  $p(x) = \exp[i(k_x x + l_x x^2)]$  and  $q(y) = \exp[i(k_y y + l_y y^2)]$  with the phase aberration matrix re-written as  $Q(x, y) = pq^H$ , where  $\{\cdot\}^H$  denotes the complex-conjugate transpose. The illuminating feature of this is the problem of phase compensation is recast as finding the first principal component of the exponential term of the filtered hologram. By decomposing the phase matrix using singular value decomposition (SVD), the dominant rank one subspace of  $Q$  can be extracted and then the linear and quadratic coefficients in  $p$  and  $q$  can then be identified independently on the unwrapped phase components of left and right dominant singular vectors using least-squares fitting. Besides, the whole algorithm can be implemented in cropped spectrum within the spatial filter (+1 order region) without any redundant data, which enables a very fast processing speed.

As an example, Figure 7 demonstrates the phase aberration compensation experimental results on macrophage cells. If one simply applies the spectrum centering procedure to the hologram, the reconstructed phase [Fig. 7(a)] shows concentric circular patterns introduced by the quadratic phase factor. Besides, the center of these concentric circles is shifted due to the residual tilt caused by improper spectrum centering (the center of the +1 order spectrum no long demonstrate a sharp peak and thus is difficult to locate automatically). The quadratic phase aberration was effectively flattened and no curved or tilted background can be perceivable when the PCA compensation method was applied, as shown in Figs. 7(b)–7(d).

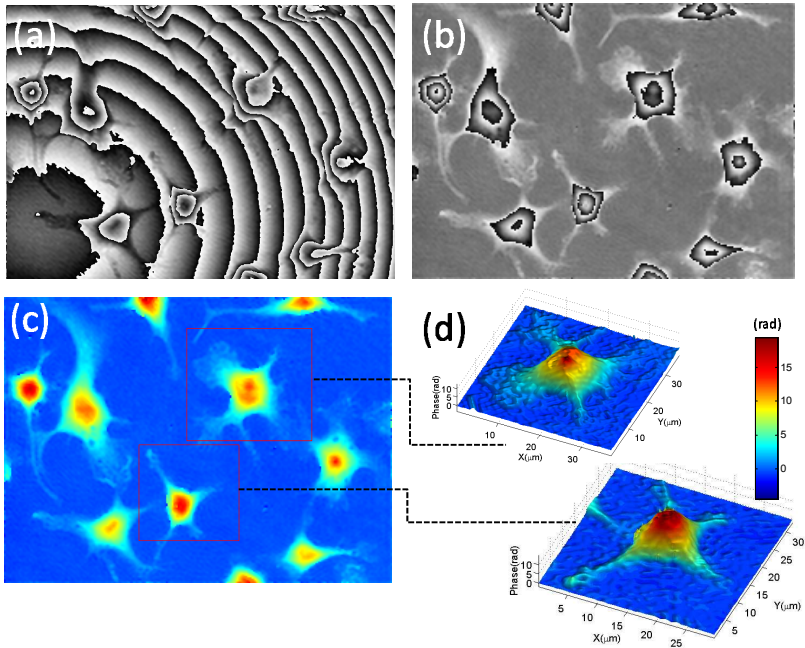


Figure 7. Phase aberration compensation using the PCA algorithm. (a) Wrapped phase map with spectrum centering only, (b) Wrapped phase map obtained after PCA phase aberration compensation. (c) Unwrapped phase map from (b). (d) Pseudo-three-dimensional plot of two individual cells indicated by red boxes in (c).

### 3. Practical Systems for Digital Holographic Microscopy

We have developed several practical holographic systems (so-called digital holoscope) with different optics configurations and for different applications. The compact digital holoscope (CDH) - a reflection type lens-less digital holography microscopic system geometry is shown in Fig. 8. A diverging laser beam from the fiber end provides the magnification in a lensless geometry. The beam is divided into two parts by using a beam splitter; one beam illuminates the sample and other incident on the plane mirror. The sample is illuminated by

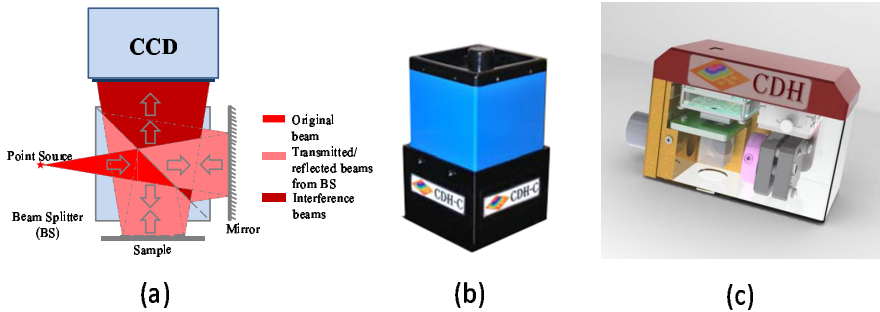


Figure 8. The Compact Digital Hologscope (CDH). (a) Optical configuration. (b) Packaged system (size:  $55\text{mm} \times 75\text{mm} \times 125\text{mm}$ ); (c) The new system integrated with the board camera.

the diverging beam, coming from the beam splitter. The scattered light from the sample (object beam) is combined with the other diverging beam, reflected from the mirror (reference beam) and the resulting interference pattern is recorded by the CCD. The divergence of the wave provides the geometrical magnification and thus improves the system resolution. This optical system is housed in a compact metal casing (box) as shown in Fig. 8(b). The illumination source is a single mode optical fiber end which provides the diverging laser beam attached to the casing. The wavelength of the light is chosen according to the application and/or the required lateral resolution. For the presented system, a fiber coupled laser diode with wavelength 642 nm is used. The premise behind this configuration is to use minimum optics to optimize the aberration and make the system very light-weight, portable and compact, enabling it to be easily integrated into other systems for various types of applications. By using a board-level camera, the total size of the system can be further shrunk by about 30%, as shown in Fig. 8(c). The newest version of the system has also incorporated the laser and the controller into the system body [Fig. 9(a)]. The measurement field of view can be further expanded by combining a motorized stage with the system, as shown in Fig. 9(b).

Another interesting non-conventional digital holography configuration - Common-Path Digital Hologscope (CPDH) is shown in Fig. 10. A single diverging spherical wave passing through the microscope objective illuminate the two adjacent sides of the beam splitter with the semi-reflecting layer ori-



Figure 9. The compact digital holoscope with the built-in laser (a), and a motorized stage (b).

ented along the optical axis with a slight tilt angle. The two halves of the beam transmit through or reflect from the opposite sides of the beam splitter's semi-reflecting hypotenuse, and then combine and exit the beam splitter forming the interference. The sample is placed in the path of one of the half beams. This common-path configuration offers advantages of simplicity, vibration insensitivity, and inherently compensated the phase curvature.

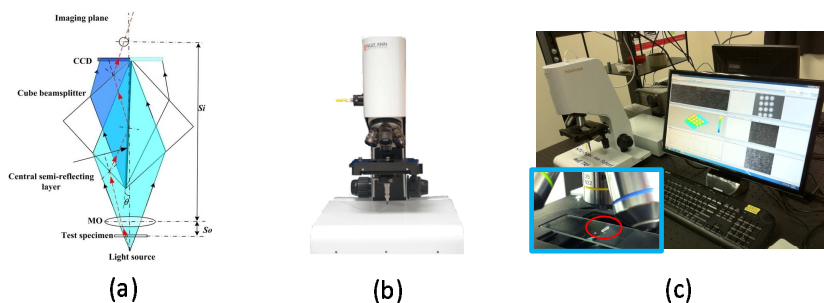


Figure 10. The Common Path Digital Holoscope (CPDH). (a) Optical configuration. (b) Packaged system. (c) The whole system under operation, the sample is a micro-lens array.

Finally, a transmission digital holographic microscopy system with the Michelson interferometer configuration is shown in Fig. 11. The beam emitted from a laser is coupled into a  $1 \times 2$  single-mode fiber coupler and then split



Figure 11. The Michelson-structure digital holoscope. (a) Optical configuration. (b) Packaged system.

into a reference wave and the object wave. Both the object wave and reference wave are combined by the cube beam splitter, and interference occurs at the plane of a CCD camera. A microscope objective is inserted in the object arm to provide the geometrical magnification and thus improves the system lateral resolution. The system is also equipped with a motorized stage.

Those digital holographic microscopy systems provide the following attractive features:

- Nanometric depth and height resolution;
- Full field analysis: line profile analysis, color maps 3D plot of sample height;
- Real-time measurement: capture live hologram and reconstruct amplitude, phase and 3D image in real-time;
- Static and dynamic analysis;
- Non-contact and non-invasive;
- User friendly software.

## 4. Applications

Featured by digital recording and numerical reconstruction, digital holography has brought the field of optical holography a big step forward to practical appli-

cations for precision quantitative phase measurement on the micro- and nano-scales in numerous and various fields. The advantages gained by the pure digital recording and processing of the hologram make digital holography an easy and versatile tool to adapt to different applications under different environment, with the accuracies comparable to interferometers, simplicity as any types of optical microscope, and providing additional information in the third dimension.

#### 4.1. MEMS and Microsystem Metrology

One important application for digital holographic microscopy is the inspection and characterization of micro-devices. The integration of mechanical elements, electronics, sensors, and actuators on a common silicon substrate by micro-machining technology constitutes micro-electro-mechanical systems (MEMSs). Inspection and characterization of MEMS during different stages of fabrication is becoming increasingly important for performance, reliability and repeatability of device. Digital holographic microscopy offer new possibilities for non-invasive inspection and characterization of the MEMS and micro-device, which are fabricated using Si-based micro-fabrication process, and usually possesses well reflectivity. digital holographic microscopy can be used to provide the feedback about the material properties, device behavior and simulation process throughout the various stages of processing, manufacturing, assembly, and testing.

##### 4.1.1. 3D-Profile Measurement

In digital holographic microscopy, the object wavefront is encoded in the hologram during the recording process through interference with a reference wavefront. The object wavefront is then retrieved by numerical reconstruction of hologram. From the digital object wavefront, its amplitude and the phase can be extracted. The amplitude provides the 2D intensity image while the phase provides the optical path length difference (OPD) which contains the 3D information of the object

$$OPD = \frac{\lambda\phi}{2\pi} = k^{-1}\phi. \quad (31)$$

For reflective specimen, such as MEMS samples, their 3D profile can be obtained by directly converting their phase map into height/depth values using

$$H(x, y) = \frac{OPD(x, y)}{2} = \frac{\lambda\phi(x, y)}{4\pi}. \quad (32)$$

Note if the measurement range is larger than half wavelength of the light source used, phase unwrapping is needed to remove the phase jumps (56). In the case when discontinuity more than half wavelength exists, spatial phase unwrapping cannot identify the phase order correctly and temporal phase unwrapping are then needed by introducing two or more wavelength illuminations.

A piezo-attenuated circular micro-membrane diaphragm is profiled using the quantitative phase information obtained from a digital holographic microscope. The diaphragm was fabricated by bonding a piezoelectric plate onto a silicon on insulator (SOI) wafer with  $20\mu\text{m}$  thick device layer. The thickness of the piezoelectric layer was thinned down to about  $40\mu\text{m}$  by using chemical/mechanical polish. The back side silicon was etched away by deep reactive ion etching. The photogram of the device is shown in Fig. 12(a), taken under a conventional bright-field reflective microscope. The hologram of the sample is shown in Fig. 12(b). The reconstructed amplitude image and phase image are shown in Figs. 12(c) and 12(d), respectively. Since the phase jumps in the wrapped phase map is more than  $2\pi$ , phase unwrapping is performed to obtain the continuous phase map, as shown in Fig. 12(e). The unwrapped phase map can be converted to the height distribution according to Eq. (32), and the color-coded 3D profile of the sample is illustrated in Fig. 12(f). It is important to note that the amplitude, phase, and 3D profile of the sample are all decoded from the single hologram. The defect on the top part of the membrane can be clearly seen from the phase image, but not observable from the conventional bright-field microscope image or the reconstructed intensity image.

#### **4.1.2. Displacement and Deformation Measurement – Digital Double Exposure Method**

The double-exposure method of holographic interferometry is a powerful tool for measuring small displacement and deformation during changes of the object state (57, 31). Single exposure interferometric method is limited to specular reflector only, while double exposure holography allowing very small motions of arbitrary, diffusely reflecting objects to be detected. In conventional double exposure interferometry, two holograms of a specimen before and after deformation are recorded on a single holographic plate. After illumination of the hologram with the reconstructed reference wave, the two slightly different waves are reconstructed at the same time. If the complex amplitude of the object

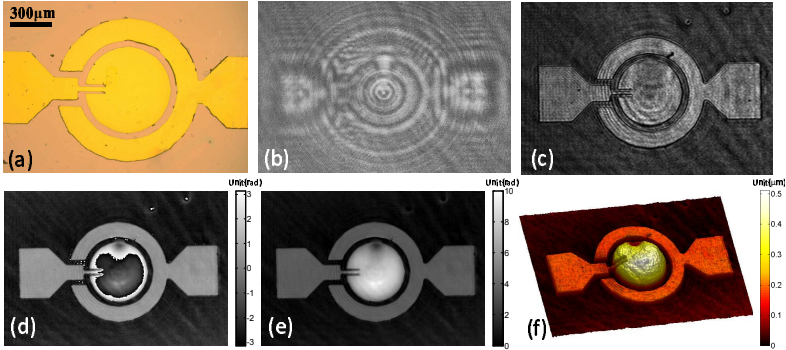


Figure 12. 3D profiling of a piezo-attenuated circular micro-membrane diaphragm. (a) Microscope image of the test sample. (b) Recorded digital hologram. (c) Reconstructed amplitude image. (d) Reconstructed wrapped phase map. (e) Unwrapped phase map. (f) Color-coded 3D rendering of height distribution.

wave in the initial state and deformed state can be represented by

$$O_1(x, y) = |O| \exp[i\phi_1(x, y)], \quad (33)$$

and

$$O_2(x, y) = |O| \exp \{i [\phi_1(x, y) + \Delta\phi_1(x, y)]\}. \quad (34)$$

The intensity of a holographic interference pattern is then can be represented as

$$I(x, y) = |O_1(x, y) + O_2(x, y)| = 2|O|^2 \{1 + \cos[\Delta\phi_1(x, y)]\}. \quad (35)$$

Note here we assume the deformation is small so that the amplitudes of the object before and after deformation are unchanged. The resulting intensity of the holographic interferogram exhibits the cosine-shaped distribution, making it difficult to retrieve the interference phase correctly from one single fringe pattern. Usually, three or more phase-shifted interferograms are required to reconstruct the phase by a phase-shifting algorithm.

In the same way, digital holography can be employed to perform double-exposure holographic interferometry. Two holograms corresponding to different states of the object are recorded and stored subsequently and then added point wisely to generate a digital double-exposure hologram (31). But to demodulate

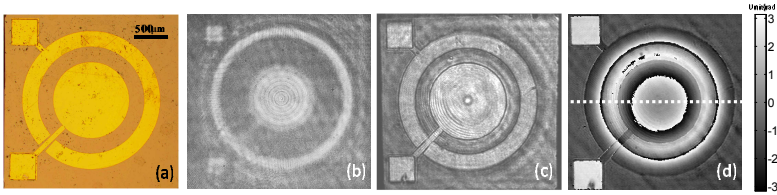


Figure 13. Thermal deformation analysis of a piezo-attenuated circular micro-diaphragm. (a) Microscope image of the test sample. (b) Recorded digital hologram at room temperature ( $25^{\circ}\text{C}$ ). (c) Reconstructed amplitude image. (d) Reconstructed wrapped phase map.

the phase information, additional experimental effort is still required. Actually, digital holography provides an alternative and much simpler way to realize double exposure interferometry. In each state of the object a digital hologram is recorded. Instead of superimposing these holograms as in conventional double-exposure method, the digital holograms are reconstructed separately according to the theory of Section 3. Direct subtraction between the two numerically reconstructed unwrapped phases provides the phase difference between the two states. Besides, if the phase difference is smaller than  $2\pi$ , the phase unwrapping can be saved. Another benefit from the digital double exposure method is the phase aberration can be simultaneously suppressed by the subtraction

The digital double exposure holographic interferometry was applied to study the thermal deformation of a piezo-attenuated circular micro-membrane diaphragm. The microscopy image of the sample is shown in Fig. 13(a). It is similar with the one shown in Fig. 12 but with different size and electrodes structure. The diaphragm is heated from room temperature ( $25^{\circ}\text{C}$ ) to  $300^{\circ}\text{C}$  by an electrical heater. The recorded hologram of the sample at room temperature is shown in Fig. 13(b). The reconstructed amplitude image and phase image are shown in Figs. 13(c) and 13(d), respectively. Since only the thermal deformation is interested in this test, the hologram at room temperature is severed as the reference. To get the deformation map at different temperature, the unwrapped phase map obtained by the holograms recorded at  $50, 100, 150, 200, 250,$  and  $300^{\circ}\text{C}$  are subtracted from the reference phase [Fig. 13(d)], and the resultant phase difference maps corresponding to the thermal deformations at different temperatures are shown in Fig. 14. The corresponding deformation 3D maps of the diaphragm are shown in Fig. 15, converted from the unwrapped

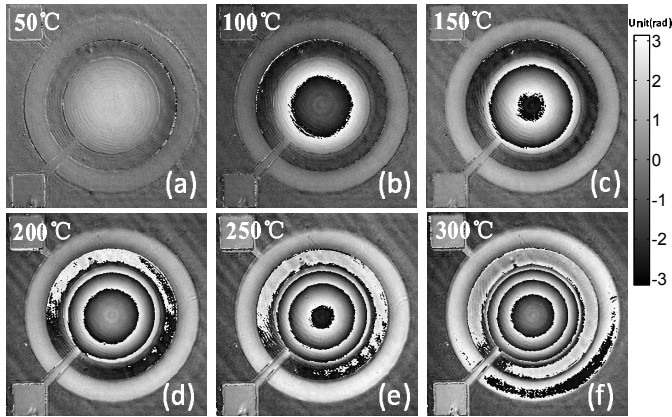


Figure 14. Wrapped phase difference maps obtained from double exposure and digital phase subtraction (a) 50 ° C, (b) 100 ° C, (c) 150 ° C, (d) 200 ° C, (e) 250 ° C, and (f) 300 ° C.

phase map by using Eq. (32). Note when the deformation is small (50 ° C), the deformation can be directly obtained from the phase difference without phase unwrapping. Figure 16 shows the cross-sections along the white dotted line indicated in Fig. 13(d). It is shown that the out-of-plane displacement of the diagram shows a circular symmetric parabolic distribution and the deformation around the central region of the diagram increases rapidly with temperature, achieving 1.09  $\mu\text{m}$  at 300 ° C. Besides, the increase rate shows a trend of rise first then fall, and the largest increase in deformation appeared between 100 ° C to 150 ° C, up to 226 nm.

#### 4.1.3. Time Average Digital Holography

Digital holographic interferometry also provides more opportunities and possibilities for fast, full field characterization of dynamic phenomenon, such as vibration. There are two approaches to this – the first is to use a pulse lasers or high-speed high-sensitivity camera to record multiple frames (7, 58), which are then, processed much like the static case described in Section 4.4.1. However, methods such as pulsed or stroboscopic digital holography require precise synchronization of the light source, the specimen and the recording device, which complicate the experimental system. The second and more interesting approach

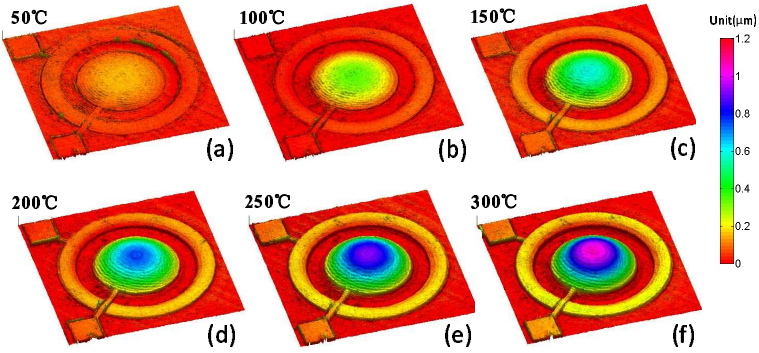


Figure 15. Color-coded 3D distributions of thermal deformation of the piezo-attenuated circular micro-diaphragm at different temperatures. (a) 50 ° C, (b) 100 ° C, (c) 150 ° C, (d) 200 ° C, (e) 250 ° C, and (f) 300 ° C.

is to use the time average method, which does not require any special camera or a pulsed laser. The principle of time averaged holographic interferometry for vibration analysis was first explained by Powell and Stetson (59). For a sinusoidally vibrating object in the  $(x, y)$  plane that the displacement passes parallel to the illumination direction [Fig. 17(a)], the instantaneous object wave  $O'(x, y, t)$  at any instant scattered from the vibrating object is:

$$O'(x, y, t) = O_0(x, y) \exp [i\phi_0(x, y)] \exp [i\Delta\phi(x, y, t)]. \quad (36)$$

Here is  $O_0(x, y)$  the complex amplitude dispersed by the object surface at rest, and  $\phi_0(x, y)$  is the phase representing the mean deformation state of the vibrating object and is called the mean static state.  $\Delta\phi(x, y, t)$  corresponds to the phase change due to the transient displacement the oscillating object, deviated from its mean static state. For a sinusoidally vibrating object, considering relations Eqs. (32) and (36), the instantaneous object wave can be written as:

$$O'(x, y, t) = O_0(x, y) \exp [i\phi_0(x, y)] \exp [ik \cdot 2z(x, y) \cos \omega t], \quad (37)$$

where  $\omega$  is the angular frequency of vibration,  $k$  is the wave number, and  $z(x, y)$  is the amplitude of vibrations in points  $(x, y)$  on the object surface.

For time averaged recording of a vibrating object, the exposure time  $\tau$  must be much larger than the period of vibration. In this case, it can be deduced that

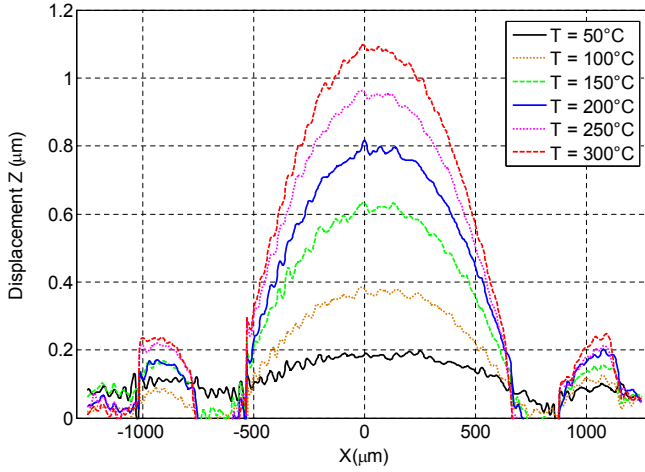


Figure 16. Line profiles of thermal deformation of the micro-diaphragm at different temperatures.

the amplitude distribution of the object is modulated by the zero order Bessel function (10, 6):

$$O(x, y) = \frac{1}{\tau} \int_0^{\tau} O'(x, y, t) d\tau = O_0(x, y) \exp[i\phi(x, y)] J_0[2kz(x, y)]. \quad (38)$$

with

$$|O(x, y)| = O_0(x, y) J_0[2kz(x, y)]. \quad (39)$$

and

$$\phi(x, y) = \phi_0(x, y) + \phi_J(x, y) \quad (40)$$

where  $J_0$  is Bessel function of the first kind and zero order,  $\phi(x, y)$  represents the phase of the object wave which is a combination of phase due to the mean static state data  $\phi_0(x, y)$  and the time-average phase  $\phi_J(x, y)$ . The  $\phi_0(x, y)$  varies from  $-\pi$  to  $\pi$  whereas  $\phi_J(x, y)$  is the binary phase (with values 0 and  $\pm\pi$ ) that changes at the zeros of the Bessel function. From Eq (39), it follows that the reconstructed amplitude contains the information of the amplitude of vibration amplitude, characterized by the Bessel function of zero order.

With the additional flexibilities provided by digital holography, time average holographic interferometry can be realized with in-line geometry, by incorporating digital double exposure method to suppress the unwanted zero-order

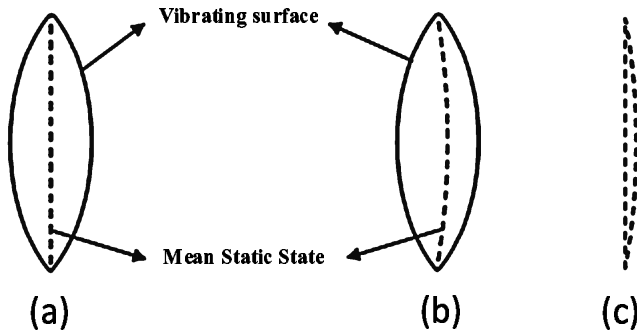


Figure 17. (a) Sinusoidally vibrating object, (b) Vibrating object with a change in the mean static state (c) Change in the mean static state.

and twin image wave. In double exposure time average digital holography, two holograms are recorded, corresponding to the reference state (either static or vibration) and the measurement state (vibration) of the object, respectively. Considering two time average holograms recorded at the same vibration frequency but with different amplitudes of vibration, according to Eqs. (38) and (39), the difference in amplitudes then provides the Bessel type vibration fringes with different visibility while the difference of phase gives the mean deformation of the object. Meanwhile, the unwanted zero-order and twin image wave is automatically suppressed during this subtraction process. Eventually the amplitude subtracted pattern used for the study of vibration amplitude information and phase subtraction provides the information about the mean static deformation of the object during vibration cycle.

Vibration analysis of an ellipse-shaped MEMS diaphragm with the major and minor axes 7 mm and 6.2 mm respectively is studied. The photograph of the MEMS diaphragm is shown in Fig. 18. The diaphragm is excited by applying an AC driving voltage across the piezoelectric layer. Double exposure holograms of the membrane are recorded at the same frequency but at slightly different amplitude. By subtraction of reconstructed intensities from two different, the mode shapes of the vibrating MEMS diaphragm can be obtained, which is modulated by the Bessel function  $J_0$ , as shown in Figs. 19(a)–19(h). The vibration modes shown in Fig. 19 can be identified as, (a) (0,1) at 14 kHz; (b) (1,1) at 29 kHz; (c) (2,1) at 45 kHz; (d) (3,1) at 70 kHz; (e) (4,1) at 90 kHz, (f) (1,2) at 105 kHz, where the number in the parentheses refers to the torsional

and bending modes.

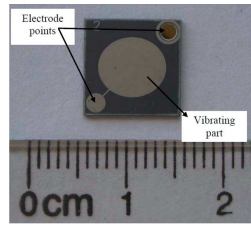


Figure 18. Photo of the MEMS diaphragm.

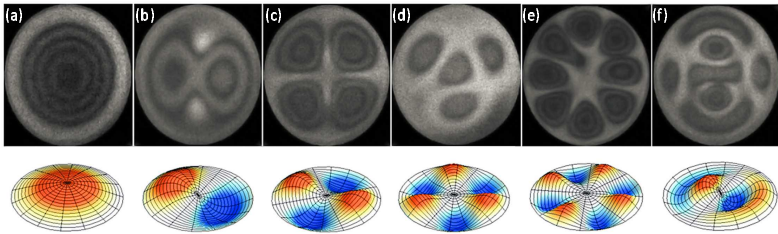


Figure 19. Vibration mode patterns reconstructed using double exposure in-line time average digital holography corresponding to the resonant frequencies (a) 14KHz, (b) 29KHz, (c) 45KHz, (d) 70KHz, (e) 90KHz, and (f) 105KHz. Their corresponding fundamental mode shapes are illustrated in the second row.

As discussed previously, the numerical reconstructed phase from time-averaged holograms contains two parts, the first part represents object surface roughness and the second part is called time average phase which shows the zeros of the function. Although the time average phase contains only binary values (with numerical values 0 and  $\pm\pi$ ), it provides a clear representation of the zeros of  $J_0$  function. For pure sinusoidal vibration of the object, the subtraction of phases of time average and reference hologram (without vibration) provides only the time average phase. This is shown in Figs. 20(a)–20(c) corresponding to the frequencies (a) 14KHz, (b) 45KHz, and (c) 105KHz. Compared to Fig. 19, all zeros of the function can be clearly identified from the time average phase. The eventual use of binary jumps is particularly useful in case of higher vibration amplitudes. It is because the time averaged amplitude fringes are modulated by zero-order Bessel function, so for higher order fringes the

contrast becomes significantly poorer, while the time average phase shows the binary jumps and thus has the same contrast for all orders.

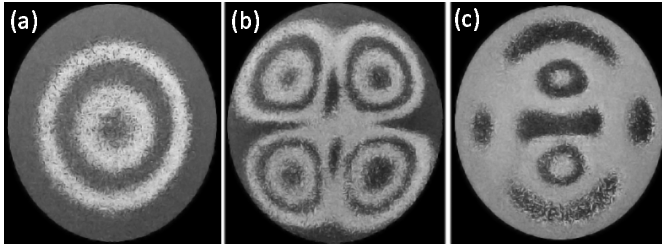


Figure 20. Time average phase representing the binary jumps corresponding to the zero of the Bessel function (a) 14KHz, (b) 45KHz, and (c) 105KHz.

## 4.2. Characterization of Micro-optics

Micro-optics is an enabling technology and plays an important role in a large variety of applications, such as consumer products, medical industry, optical sensors, micro-electronics, laser micro-machining and materials processing, optical inspection, machine vision, precision metrology, etc. Various applications and their subsequent requirements with respect to cost structure, accuracy, quality and lifetime, caused different manufacturing technologies to evolve in the last decades. However, precise control, inspection and testing the micro-optics product are still challenging tasks.

The micro-optical component mainly includes microlens array, diffractive optical element (DOE), and binary optics element (BOE). Microlens array based on the refraction or diffraction principle is composed by a series of microlens with the size from several microns to hundred microns, which is characteristic by small size, little transmission loss, and convenient large-scale manufacture. The geometrical characterization of microlens array, especially the shape, surface roughness, and the radius of curvature influenced its optical performance imaging quality significantly. Many different metrology approaches are applicable to obtain the geometrical profiles of the micro-optics elements.

Contact techniques, based on a sensitive detection stylus that scans the microlens surface along a line, have a limited accuracy due to the shape and size of the stylus tip. Confocal microscopy is a noncontact technique used for micro-optics characterization. It is based on scanning and, thus, has a slow measure-

ment speed. Other noncontact techniques are based on interferometry, such as the Twyman-Green interferometer, Mach-Zehnder interferometer, and white light interferometer. These methods have some common drawbacks of a relatively low measurement speed due to the phase-shifting procedures and cannot characterize strong aspherical and nonspherical (e.g., cylindrical) lenses.

Digital holography provides a simple, effective, and non-contact way to profile the micro-optics with advantages of single acquisition, full field, and high speed (19, 20, 60). When the light wave passes through a semi-transparent or transparent micro-optical component, its phase will carry the profile information and can be converted to physical thickness according to Eq. (41).

$$T(x, y) = \frac{OPD(x, y)}{\Delta n} = \frac{\lambda}{n_o - n_m} \frac{\phi(x, y)}{2\pi}. \quad (41)$$

where  $\Delta n$  is the difference between the refractive index of test object  $n_o$  and the medium around the test object  $n_m$ . The medium is commonly air, thus  $n_m$  is approximated to 1. Therefore, with a known refractive index of the lens material, the geometric profile, as well as the lens height, length, and the radius of curvature can be easily obtained from the phase map.

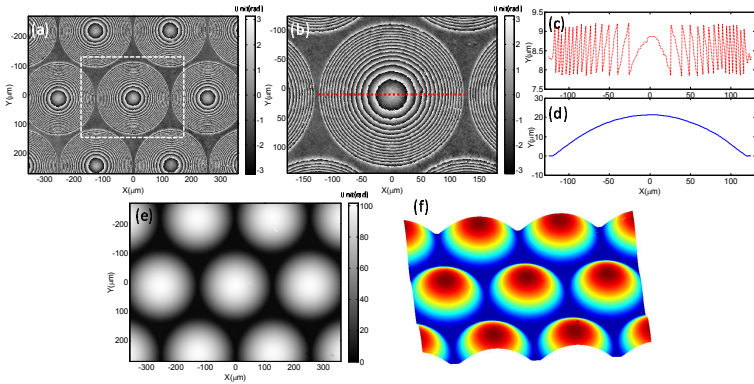


Figure 21. Phase measurement results of a plano-convex quartz microlens array with (pitch  $250 \mu\text{m}$ ). (a) Unwrapped phase map. (b) Enlarged region corresponding to the white dashed box in (a). (c) Line profile along the red dotted line in (b). (d) Line profile of the thickness of single microlens. (e) Unwrapped phase map. (f) 3D rendering of phase distribution.

Figure 21 presents the measurements of a plano-convex quartz microlens ar-

ray with  $250\ \mu\text{m}$  pitch by using a common path digital holographic microscope. The microlens array is from from SUSS MicroOptics and each microlens in the array has a diameter of  $240\ \mu\text{m}$ . Figure 21(a) present the reconstructed wrapped phase map with the enlarged central region for one single microlens shown in Fig. 21(b). As can be seen in Fig. 21(b), the unwrapped phase map demonstrate highly dense phase jumps and an unwrapping algorithm is needed to retrieve the continuous phase, as shown in Fig. 21(e). The 3D rendering of unwrapped phase distribution is presented in Fig. 21(f). Note that to ensure the unwrapping algorithm works, the magnification of the microscope objective employed should be sufficiently high so that the phase jumps can be laterally resolved without aliasing distortion. Two line profiles of the wrapped and unwrapped phase map extracted from the center of the lens are presented in Figs. 21(c) and 21(d), corresponding to the red-dot line shown in Fig. 21(b).

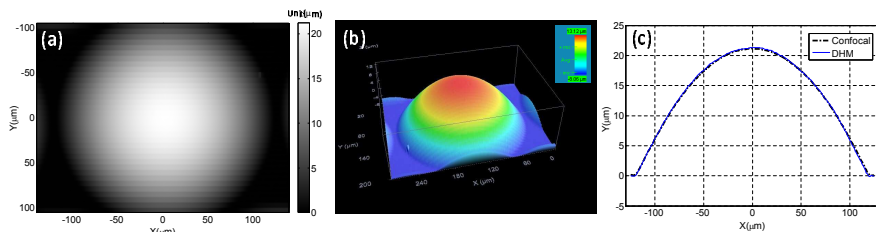


Figure 22. Comparison with confocal microscopy. (a) Height distribution of a single microlens measured by using a commercial white-light scanning confocal microscope (b) 3D topography. (c) comparison of the cross-sections along the same line in Fig. 6 (b).

To further validate the quantitative results obtained by digital holographic microscopy, we compare the results with confocal microscopy. Figure 22 presents the height distribution and 3D topography of a single microlens measured by using a commercial white-light scanning confocal microscope. The cross-sections along the same line in Fig. 21(b) are compared in Fig. 22(c), which demonstrate a good concordance with the digital holographic microscopy result. Given the height profile of the lens, the radius of curvature (ROC) can be calculated by

$$ROC = h/2 + D^2/8h, \quad (42)$$

where  $h$  is the height of the microlens, and  $D$  is the diameter of the microlens. The maximal height  $h$  of the microlens are measured  $21.31\ \mu\text{m}$  for digital holo-

graphic microscopy and  $21.19\mu\text{m}$  for confocal microscope. Thus, the calculated ROC are  $348.5\mu\text{m}$  for digital holographic microscopy and  $350.4\mu\text{m}$  for confocal microscope, which both correspond well to manufacturer specifications ( $350\mu\text{m}$ )

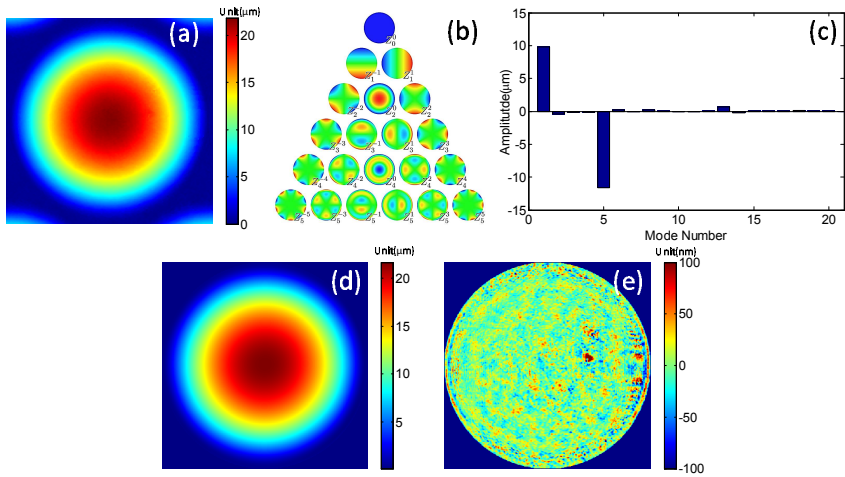


Figure 23. Aberration and roughness analysis using Zernike expansion (a) Raw topography of individual microlens of the same microlens measured by digital holographic microscopy. (b) The first 21 Zernike functions used as basis for decomposition. (c) Calculated Zernike coefficients. (d) Reconstructed microlens topology, using the 21 Zernike coefficients shown in (c). (e) fitting residual.

To accurately quantify the aberrations in optical wavefront related to the shape of the lens profile, Zernike polynomials expansion analysis can be carried out on the reconstructed height distribution. The analysis consists the automatic location of the centers of the microlens, choosing the valid region of the lens and applying Zernike expansion method. The exemplary results are presented in Fig. 23. The Zernike decomposition of was carried out on the individual microlens shown in Fig. 21(a). We use the first 21 modes, which correspond to the degree of the Zernike functions from 0 to 7, as illustrated in Fig. 23(b). Figure 23(c) shows the computed coefficients. It can be seen that apart from 1st constant offset term ( $Z_{00}$ ), and the 5th defocus term ( $Z_2$ ), the dominant modes in the data is the 13th spherical aberration term ( $Z_{42}$ ). The Seidel aberrations such as astigmatism, coma do not play a significant role and there were negligible con-

tributions from some higher order terms. The reconstructed topology data from the computed 21 Zernike coefficients are shown in Fig. 32(d). Qualitatively, the agreement between the original and the reconstructed data is very good. The fitting residual shown in Fig. 23(e), which is the difference between the original and reconstructed data, provides information about the surface roughness of the microlens (the average roughness of the microlens is 15.09 nm).

Three more examples are further provided in Fig. 24. In Figs. 24(a)–24(c), we show the measurement result of another plano-convex quartz microlens array with 100  $\mu\text{m}$  pitch. In addition to spherical microlens, a wide variety of other micro-optics components can be successfully characterized by digital holographic microscopy. For example, Fig. 24(d)–24(f) present results obtained with a cylindrical lens with 35  $\mu\text{m}$  diameter, and Figs. 24(g)–24(i) provide the measurement results of a binary diffractive optical element.

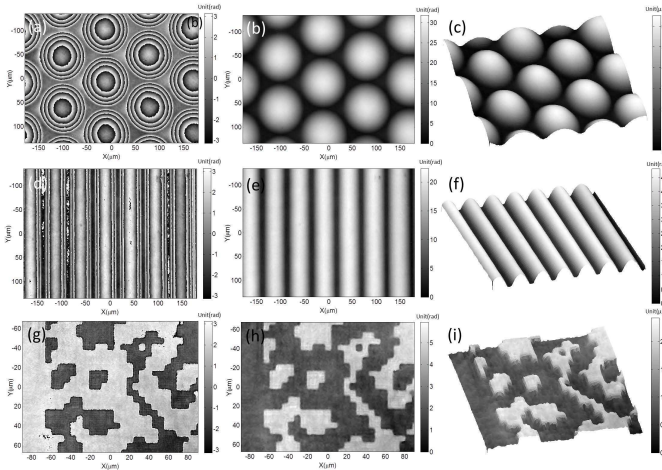


Figure 24. Digital holographic microscopy results of different types of micro-optics components. First row: a 100  $\mu\text{m}$  pitch plano-convex quartz microlens array. Second row: a cylindrical lens with 35  $\mu\text{m}$  diameter. Third row: a binary diffractive optical element. The wrapped phase map, unwrapped phase map, and the 3D map of height distribution are respectively given in the first, second, and third column.

### 4.3. Quantitative Phase Contrast Bio-imaging

Individual cells and biological tissues are often challenging samples for optical microscopy since they are largely transparent and offer low contrast when viewed under light illumination. Consequently, stains and fluorescent dyes are frequently used to enhance contrast but can often disrupt the health of living cells. An alternative is to directly image the refractive index contrast of the cell with its background to produce a phase image. Zernike phase contrast (61) and differential interference contrast microscopy (62) have proven to be extremely powerful imaging tools for visualization of phase variation. However, in general the phase information through such means is neither linear nor quantitative, yielding only qualitative descriptions in terms of optical path-length measurement.

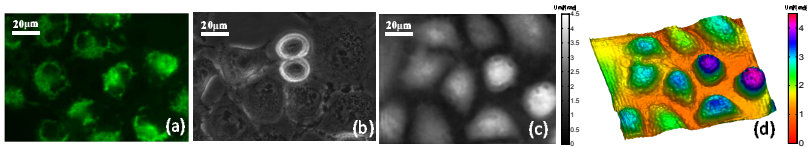


Figure 25. Comparison of a fluorescence microscopy image (a), Zernike phase contrast microscopy image (b), and digital holographic microscopy image (c). (d) is the 3D rendering of (c).

Digital holography brings unique possibilities for biological sample investigations since it is able to reconstruct simultaneously an amplitude-contrast and a phase-contrast image, making it possible to easily measure cell properties that previously have been very difficult to study in living cells, such as cell thickness, volume, and cell refractive index (23, 24). Quantifying the optical phase shifts associated with phase samples gives access to information about cell morphologies that can be used further for quantitative studies. In Fig. 25(a), human nasopharyngeal carcinoma cells CNE2 are captured using fluorescence microscopy (cells stained with fluorescein isothiocyanate), Zernike phase contrast microscopy, and digital holographic microscopy. Zernike phase contrast render the phase of living biological cells visible without staining, however, it always exhibit halo artifacts which can be easily observed in Fig. 25(b), as bright contours around dark specimens. This halo artifact is the result of diffracted light passing through the phase ring as well as the non-phase areas and interacting at the image plane. Without artificial structure and distortion,

digital holographic microscopy creates a quantitative phase shift image showing the optical thickness of the object [Fig. 25(c)], thus makes it much easier to visualize, quantify, and analyze the actual structure of the specimen. Figure 25(d) shows the pseudo-3D view of the quantitative phase map, which conveys quantitative information about the physical thickness and index of refraction of the cells.

It should be noted that according to Eq. (41), the magnitude of the phase shift induced by the cell depends on the refractive index of the cell and the cell thickness as well as the difference in refractive index between the cells and their surroundings. For certain cells such as mature red blood cells, in which a constant refractive index can be assumed for the entire cell contents (e.g.,  $n_c \cong 1.395$ ), the thickness profile can be directly obtained from the phase profile. If the refractive index is unknown, the decoupling procedure is needed to separate integral refractive index and the cellular thickness from the quantitative phase images of living cells (63). For heterogeneous cells that contain organelles with different refractive indices, the thickness and refractive both conjugate in the phase profile, in this case, dry mass, which can be obtained directly from the phase profile can be used for quantitative analysis (64), otherwise, a uniform refractive index has to be assumed for converting to phase map into physical thickness (65, 66).

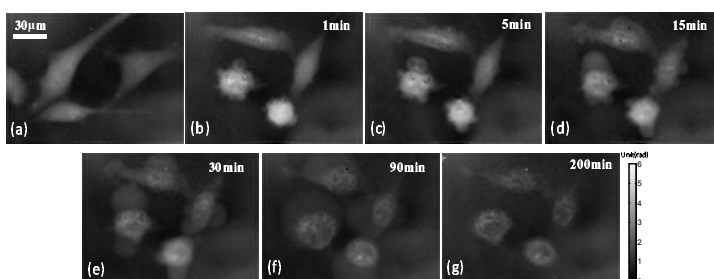


Figure 26. Quantitative phase images of CNE cells with PDT induced apoptosis. (a) Before PDT, (b) 1min, (c) 5min, (d) 15min, (e) 30min, (f) 90min, (g) 200min.

Investigation of living human nasopharyngeal carcinoma cells CNE2 were carried out to demonstrate the potential of digital holographic microscopy for the visualization of morphology changes induced by photodynamic therapy (PDT). PDT is a novel approach to treat a variety of tumors and diseases char-

acterized by abnormal cell growth, uses a photosensitizing drug, followed by irradiation with light of an appropriate wavelength, to induce cell death. CNE2 cells were cultured in Roswell Park Memorial Institute (RPMI) 1640 medium (Invitrogen, Carlsbad, CA) supplemented with 10% fetal bovine serum, 2 mM glutamine, 1mM non-essential amino acids, 1 mM sodium pyruvate, and 100 U/ml penicillin in a 5% CO<sub>2</sub>, 95% air, 37 ° C humidified incubator. As one of the most effective and extensively-studied photosensitizer for PDT, 1.25  $\mu$ M hypericin was diluted and added to culture medium. The cells were incubated in a chamber slide for 16 hours, and then placed on the stage incubator of the digital holographic microscopic system for continuous monitor. Figure 26 shows the quantitative phase images obtained before PDT and at different time points after PDT. From Fig 26, blebs were seen to start forming on the cell membrane immediately after PDT. Then the cells swelling in bubble form as well as nuclear condensation, can be clearly observed. After 200 min, all the cells seemed collapsed and plasma membrane seemed permeabilised. The overall phase contract decrease significantly. The limited regions showing larger phase values were probably due to the condensation of nuclear chromatin. During the whole process, the numerical focusing property of digital holographic microscopy permits in-focus measurements over time. Those results demonstrate that the digital holographic microscopy is an ideal tool for real-time, or time-lapse cell monitoring, allowing non-invasive, high-resolution imaging of living cells at a nanometric scale resolution from a single image acquisition.

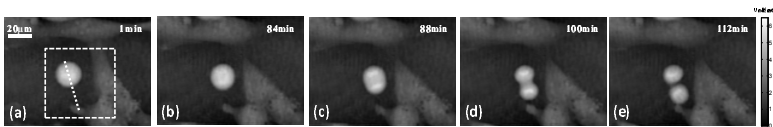


Figure 27. Time-dependent quantitative phase contrast images of living vero cells during cell division. (a) Interphase  $t = 1$  min. (b) Prophase  $t = 84$  min. (c) Metaphase  $t = 88$  min (e) Telophase  $t = 100$  min (e) Separation of two daughter cells  $t = 112$  min.

We further demonstrate the use of digital holographic microscopy for the quantitative analysis cellular morphological changes during division. 100% confluent vero cells from a T25 flask were trypsinized and diluted ten times into two T25 flasks to a final culture volume of 10ml. The flasks were inoculated at 37 ° C with 5% CO<sub>2</sub> for 12 hours to allow adherence of monolayer

cells. The quantitative phase map of vero cells during cell division are shown in Fig. 27. Figure 28 shows the color-coded pseudo-3D representation of the quantitative contrast images corresponding to the boxed region shown in Fig. 27(a). In Fig. 28(f), we draw the cross-sections through the cell thickness along the dotted line in Fig. 27(a). Note that a constant refractive index ( $n_{cell}=1.39$ , and  $n_{medium}=1.33$ ) is assumed for the entire cell contents for simplicity, so the thickness profile is directly proportionate to the phase profile.

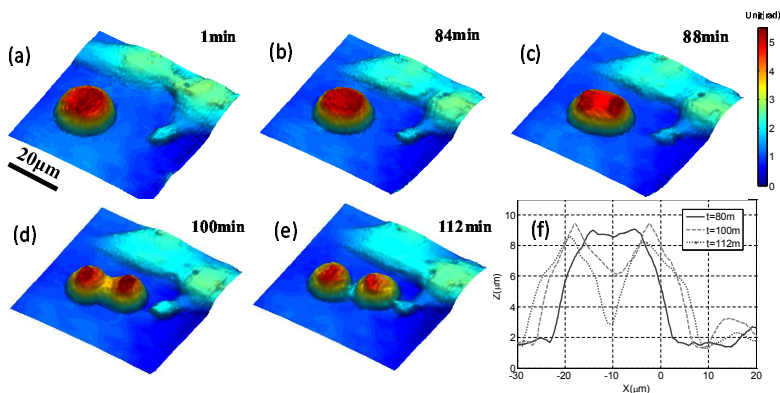


Figure 28. Color-coded pseudo-3D representation of the quantitative contrast images of living vero cell corresponding to the boxed region shown in Fig. 27. (a)  $t = 1$  min; (b)  $t = 84$  min; (c)  $t = 88$  min; (e)  $t = 100$  min; (e)  $t = 112$  min; (f) Cross-sections through the cell thickness along the dotted line in Fig. 27(a).

It was observed that prior to the cell division; cell rounding was induced, which results in a significant higher phase contrast and the cell thickness compared with the adjacent ones. This stage is called interphase, indicating the cell prepares for division. At  $t=84$  min, the cell entered into prophase, characterized by chromosomes line up at the center of the cell. Then the chromosome divided and moved to each daughter cell during metaphase stage. As is clearly shown in Figs. 27(c) and 27(d), areas with higher phase contrast indicate the separation of the chromosomes. At  $t=100$  min, the cytoplasm divided and cell wall pinches in to form the two new daughter cells, corresponding to telophase or cytokinesis stage. Finally, two individual daughter cells were formed from a single parent cell at  $t=112$  min. The daughter cells are almost identical to one another both in shape and in thickness. These results demonstrate the applicability and effectiveness of digital holographic microscopy for quantitative monitoring of the

cell division processes during long-term time-lapse observations.

## 5. Conclusion

In this chapter, we have presented the basic principle and recent developments of digital holography for applications in MEMS inspection, micro-optics characterization and quantitative phase contrast bio-imaging. Different types of recording geometries and reconstruction algorithms are reviewed. We have also present several experimental results that demonstrate the capabilities of digital holography for various applications in science and engineering. For material science, micro- and nanotechnologies, MEMS and microsystem, digital holography microscopy is performing almost ideally in many conditions: It can provide precise, absolute, and calibrated data, rendering possible the quantitative comparison with a certain gauge and standard; it can be designed compact enough which allow measurements being made on-line during the fabrication stage; it can be rapidly adapted to changing requirements because of its flexibility provided by digital processing. For micro-optics testing, digital holography offers the great advantage in measuring small lens structures with a very compact and simple geometry. Several biological applications, such as morphology and functional studies have been already proved that digital holography microscopy technology will bring quantitative phase information with fast imaging capabilities, non-scanning and non-invasive features. Digital holography is no longer an unfamiliar term and now poised to move out of the lab and into industry. Due to its unique advantages such as: 3D information extraction with single-shot imaging, digital refocusing, flexibility in aberration correction, simplified configuration, and low cost etc., we firmly believed that the digital holography will demonstrate even larger potentials in diverse fields in further development.

## Acknowledgments

This work was supported by the Research Fund for the Doctoral Program of Ministry of Education of China (20123219110016), the National Natural Science Foundation of China (61271332), and the Fundamental Research Funds for the Central Universities (30915011318). C. Zuo thanks the support of the 'Zijin Star' program of Nanjing University of Science and Technology.

## References

- [1] G. D., A new microscopic principle, *Nature* 161, 777–778 (1948).
- [2] M. Kronrod, N. Merzlyakov, and L. Yaroslavskii, Reconstruction of a hologram with a computer, *Soviet Physics Technical Physics* 17, 333 (1972).
- [3] U. Schnars and W. Jüptner, Direct recording of holograms by a ccd target and numerical reconstruction, *Appl. Opt.* 33, 179–181 (1994).
- [4] L. Xu, X. Peng, J. Miao, and A. K. Asundi, Studies of digital microscopic holography with applications to microstructure testing, *Appl. Opt.* 40, 5046–5051 (2001).
- [5] S. Seebacher, W. Osten, and W. P. O. Jueptner, *Measuring shape and deformation of small objects using digital holography*, (1998).
- [6] A. Asundi and V. R. Singh, Time-averaged in-line digital holographic interferometry for vibration analysis, *Appl. Opt.* 45, 2391–2395 (2006).
- [7] S. Schedin, G. Pedrini, H. J. Tiziani, and F. M. Santoyo, Simultaneous three-dimensional dynamic deformation measurements with pulsed digital holography, *Appl. Opt.* 38, 7056–7062 (1999).
- [8] P. Picart, J. Leval, D. Mounier, and S. Gougeon, Time-averaged digital holography, *Opt. Lett.* 28, 1900–1902 (2003).
- [9] P. Picart, J. Leval, D. Mounier, and S. Gougeon, Some opportunities for vibration analysis with time averaging in digital fresnel holography, *Appl. Opt.* 44, 337–343 (2005).
- [10] V. R. Singh, J. Miao, Z. Wang, G. Hegde, and A. Asundi, Dynamic characterization of {MEMS} diaphragm using time averaged in-line digital holography, *Optics Communications* 280, 285 – 290 (2007).
- [11] Y. Morimoto, T. Nomura, M. Fujigaki, S. Yoneyama, and I. Takahashi, Deformation measurement by phase-shifting digital holography, *Experimental Mechanics* 45, 65–70 (2005).

- 
- [12] G. Pedrini and H. Tiziani, Quantitative evaluation of two-dimensional dynamic deformations using digital holography, *Optics and Laser Technology*, 249 – 256 (1997).
- [13] S. Seebacher, W. Osten, T. Baumbach, and W. Japtner, The determination of material parameters of microcomponents using digital holography, *Optics and Lasers in Engineering* 36, 103 – 126 (2001). Osten Microsystems Metrology (Part 1).
- [14] E. CuChe, F. Bevilacqua, and C. Depeursinge, Digital holography for quantitative phase-contrast imaging, *Opt. Lett.* 24, 291–293 (1999).
- [15] I. Yamaguchi, S. Ohta, and J. ichi Kato, Surface contouring by phase-shifting digital holography, *Optics and Lasers in Engineering* 36, 417 – 428 (2001). Osten microsystems metrology (part 2).
- [16] I. Yamaguchi, T. Ida, and M. Yokota, *Surface shape measurement by phase-shifting digital holography with dual wavelengths*, (2006).
- [17] B. Javidi and T. Nomura, Securing information by use of digital holography, *Opt. Lett.* 25, 28–30 (2000).
- [18] E. Tajahuerce and B. Javidi, Encrypting three-dimensional information with digital holography, *Appl. Opt.* 39, 6595–6601 (2000).
- [19] F. Charrière, J. Kühn, T. Colomb, F. Montfort, E. CuChe, Y. Emery, K. Weible, P. Marquet, and C. Depeursinge, Characterization of microlenses by digital holographic microscopy, *Appl. Opt.* 45, 829–835 (2006).
- [20] Q. Weijuan, C. O. Choo, Y. Yingjie, and A. Asundi, Microlens characterization by digital holographic microscopy with physical spherical phase compensation, *Appl. Opt.* 49, 6448–6454 (2010).
- [21] D. Dirksen, H. Droste, B. Kemper, H. Deler, M. Deiwick, H. Scheld, and G. von Bally, Lensless fourier holography for digital holographic interferometry on biological samples, *Optics and Lasers in Engineering* 36, 241 – 249 (2001).
- [22] C. Oh, S. O. Isikman, B. Khademhosseini, and A. Ozcan, On-chip differential interference contrast microscopy using lensless digital holography, *Opt. Express* 18, 4717–4726 (2010).

- [23] C. Mann, L. Yu, C.-M. Lo, and M. Kim, High-resolution quantitative phase-contrast microscopy by digital holography, *Opt. Express* 13, 8693–8698 (2005).
- [24] C. J. Mann, P. R. Bingham, V. C. Paquit, and K. W. Tobin, Quantitative phase imaging by three-wavelength digital holography, *Opt. Express* 16, 9753–9764 (2008).
- [25] B. Javidi and E. Tajahuerce, Three-dimensional object recognition by use of digital holography, *Opt. Lett.* 25, 610–612 (2000).
- [26] B. Javidi and D. Kim, Three-dimensional-object recognition by use of single-exposure on-axis digital holography, *Opt. Lett.* 30, 236–238 (2005).
- [27] P. Ferraro, S. Grilli, D. Alfieri, S. D. Nicola, A. Finizio, G. Pierattini, B. Javidi, G. Coppola, and V. Striano, Extended focused image in microscopy by digital holography, *Opt. Express* 13, 6738–6749 (2005).
- [28] T. Colomb, N. Pavillon, J. Kühn, E. Cuhe, C. Depeursinge, and Y. Emery, Extended depth-of-focus by digital holographic microscopy, *Opt. Lett.* 35, 1840–1842 (2010).
- [29] G. Pan and H. Meng, Digital holography of particle fields: reconstruction by use of complex amplitude, *Appl. Opt.* 42, 827–833 (2003).
- [30] S. Murata and N. Yasuda, Potential of digital holography in particle measurement, *Optics and Laser Technology* 32, 567 – 574 (2000). Optical methods in heat and fluid flow.
- [31] T. M. Kreis, M. Adams, and W. P. O. Jueptner, *Digital in-line holography in particle measurement*, (1999).
- [32] E. Darakis, T. Khanam, A. Rajendran, V. Kariwala, T. J. Naughton, and A. K. Asundi, Microparticle characterization using digital holography, *Chemical Engineering Science* 65, 1037 – 1044 (2010).
- [33] B. Javidi, I. Moon, S. Yeom, and E. Carapezza, Three-dimensional imaging and recognition of microorganism using single-exposure on-line (seol) digital holography, *Opt. Express* 13, 4492–4506 (2005).
- [34] T. Zhang and I. Yamaguchi, Three-dimensional microscopy with phase-shifting digital holography, *Opt. Lett.* 23, 1221–1223 (1998).

- 
- [35] P. Ferraro, S. D. Nicola, A. Finizio, G. Coppola, S. Grilli, C. Magro, and G. Pierattini, Compensation of the inherent wave front curvature in digital holographic coherent microscopy for quantitative phase-contrast imaging, *Appl. Opt.* 42, 1938–1946 (2003).
- [36] T. Colomb, J. Kühn, F. Charrière, C. Depeursinge, P. Marquet, and N. Aspert, Total aberrations compensation in digital holographic microscopy with a reference conjugated hologram, *Opt. Express* 14, 4300–4306 (2006).
- [37] Q. Weijuan, Y. Yingjie, C. O. Choo, and A. Asundi, Digital holographic microscopy with physical phase compensation, *Opt. Lett.* 34, 1276–1278 (2009).
- [38] C. Zuo, Q. Chen, W. Qu, and A. Asundi, Phase aberration compensation in digital holographic microscopy based on principal component analysis, *Opt. Lett.* 38, 1724–1726 (2013).
- [39] M.-K. Kim, Tomographic three-dimensional imaging of a biological specimen using wavelength-scanning digital interference holography, *Opt. Express* 7, 305–310 (2000).
- [40] F. Charrière, A. Marian, F. Montfort, J. Kuehn, T. Colomb, E. Cuche, P. Marquet, and C. Depeursinge, Cell refractive index tomography by digital holographic microscopy, *Opt. Lett.* 31, 178–180 (2006).
- [41] P. Ferraro, S. Grilli, L. Miccio, D. Alfieri, S. D. Nicola, A. Finizio, and B. Javidi, Full color 3-d imaging by digital holography and removal of chromatic aberrations, *J. Display Technol.* 4, 97–100 (2008).
- [42] K. Maeno, N. Fukaya, O. Nishikawa, K. Sato, and T. Honda, *Electroholographic display using 15mega pixels lcd*, (1996).
- [43] F. Yaraş, H. Kang, and L. Onural, Circular holographic video display system, *Opt. Express* 19, 9147–9156 (2011).
- [44] E. Cuche, P. Marquet, and C. Depeursinge, Spatial filtering for zero-order and twin-image elimination in digital off-axis holography, *Appl. Opt.* 39, 4070–4075 (2000).

- [45] I. Yamaguchi and T. Zhang, Phase-shifting digital holography, *Opt. Lett.* 22, 1268–1270 (1997).
- [46] D. Malacara, *Optical Shop Testing*, vol. 59 (John Wiley & Sons, 2007).
- [47] K. Hibino, K. Larkin, B. F. Oreb, and D. I. Farrant, Phase shifting for nonsinusoidal waveforms with phase-shift errors, *J. Opt. Soc. Am. A* 12, 761–768 (1995).
- [48] K. Freischlad and C. L. Koliopoulos, Fourier description of digital phase-measuring interferometry, *J. Opt. Soc. Am. A* 7, 542–551 (1990).
- [49] Y. Surrel, Design of algorithms for phase measurements by the use of phase stepping, *Appl. Opt.* 35, 51–60 (1996).
- [50] J. W. Goodman *et al.*, *Introduction to Fourier optics*, vol. 2 (McGraw-hill New York, 1968).
- [51] W. Qu, C. O. Choo, V. R. Singh, Y. Yingjie, and A. Asundi, Quasi-physical phase compensation in digital holographic microscopy, *J. Opt. Soc. Am. A* 26, 2005–2011 (2009).
- [52] T. Colomb, F. Montfort, J. Kühn, N. Aspert, E. CuChe, A. Marian, F. Charrière, S. Bourquin, P. Marquet, and C. Depeursinge, Numerical parametric lens for shifting, magnification, and complete aberration compensation in digital holographic microscopy, *J. Opt. Soc. Am. A* 23, 3177–3190 (2006).
- [53] L. Miccio, D. Alfieri, S. Grilli, P. Ferraro, A. Finizio, L. De Petrocellis, and S. D. Nicola, Direct full compensation of the aberrations in quantitative phase microscopy of thin objects by a single digital hologram, *Applied Physics Letters* 90, 041104–041104–3 (2007).
- [54] J. Di, J. Zhao, W. Sun, H. Jiang, and X. Yan, Phase aberration compensation of digital holographic microscopy based on least squares surface fitting, *Optics Communications* 282, 3873–3877 (2009).
- [55] E. CuChe, P. Marquet, and C. Depeursinge, Simultaneous amplitude-contrast and quantitative phase-contrast microscopy by numerical reconstruction of fresnel off-axis holograms, *Appl. Opt.* 38, 6994–7001 (1999).

- 
- [56] D. C. Ghiglia and M. D. Pritt, *Two-dimensional phase unwrapping: theory, algorithms, and software* (Wiley New York:, 1998).
- [57] C. M. Vest, *Holographic interferometry*, New York, John Wiley and Sons, Inc., 1979. 476 p. 1 (1979).
- [58] G. Pedrini, W. Osten, and M. E. Gusev, High-speed digital holographic interferometry for vibration measurement, *Appl. Opt.* 45, 3456–3462 (2006).
- [59] R. L. Powell and K. A. Stetson, Interferometric vibration analysis by wavefront reconstruction, *J. Opt. Soc. Am.* 55, 1593–1597 (1965).
- [60] W. Qu, O. C. Chee, Y. Yu, and A. Asundi, Characterization and inspection of microlens array by single cube beam splitter microscopy, *Appl. Opt.* 50, 886–890 (2011).
- [61] F. Zernike, How i discovered phase contrast, *Science* 121, 345–349 (1955).
- [62] G. Nomarski, Differential microinterferometer with polarized waves, *J. Phys. Radium* 16, 9s–13s (1955).
- [63] B. Rappaz, P. Marquet, E. Cuhe, Y. Emery, C. Depeursinge, and P. Magistretti, Measurement of the integral refractive index and dynamic cell morphology of living cells with digital holographic microscopy, *Opt. Express* 13, 9361–9373 (2005).
- [64] B. Rappaz, E. Cano, T. Colomb, J. Kahn, C. Depeursinge, V. Simanis, P. J. Magistretti, and P. Marquet, Noninvasive characterization of the fission yeast cell cycle by monitoring dry mass with digital holographic microscopy, *Journal of Biomedical Optics* 14, 034049–034049–5 (2009).
- [65] C. Zuo, Q. Chen, W. Qu, and A. Asundi, High-speed transport-of-intensity phase microscopy with an electrically tunable lens, *Opt. Express* 21, 24060–24075 (2013).
- [66] C. Zuo, Q. Chen, W. Qu, and A. Asundi, Noninterferometric single-shot quantitative phase microscopy, *Opt. Lett.* 38, 3538–3541 (2013).